

Article

CoMnO_x Nanoflower-Based Smartphone Sensing Platform and Virtual Reality Display for Colorimetric Detection of Ziram and Cu²⁺

Chang Song^{1,†}, Fangfang Wang^{2,†}, Xin Zhang¹, Yuanxia Ma¹, Yangyu Wu³, Mingxia He², Xiangheng Niu^{3,*}
and Mengmeng Sun^{2,*}

¹ School of Arts and Media, Sichuan Agricultural University, Chengdu 611130, China

² College of Science, Sichuan Agricultural University, Ya'an 625014, China

³ School of Public Health, Hengyang Medical School, University of South China, Hengyang 421001, China

* Correspondence: niuxiangheng@usc.edu.cn (X.N.); 14391@sicau.edu.cn (M.S.)

† These authors contributed equally to this work.

Abstract: Transition metal doping is an ideal strategy to construct multifunctional and efficient nanozymes for biosensing. In this work, a metal-doped CoMnO_x nanozyme was designed and synthesized by hydrothermal reaction and high-temperature calcination. Based on its oxidase activity, an “on-off-on” smartphone sensing platform was established to detect ziram and Cu²⁺. The obtained flower-shaped CoMnO_x could exhibit oxidase-, catalase-, and laccase-like activities. The oxidase activity mechanism of CoMnO_x was deeply explored. O₂ molecules adsorbed on the surface of CoMnO_x were activated to produce a large amount of O₂^{•-}, and then, O₂^{•-} could extract acidic hydrogen from TMB to produce blue oxTMB. Meanwhile, TMB was oxidized directly to the blue product oxTMB via the high redox ability of Co species. According to the excellent oxidase-like activity of CoMnO_x, a versatile colorimetric detection platform for ziram and Cu²⁺ was successfully constructed. The linear detection ranges for ziram and Cu²⁺ were 5–280 μM and 80–360 μM, and the detection limits were 1.475 μM and 3.906 μM, respectively. In addition, a portable smartphone platform for ziram and Cu²⁺ sensing was established for instant analysis, showing great application promise in the detection of real samples including environmental soil and water.



Citation: Song, C.; Wang, F.; Zhang, X.; Ma, Y.; Wu, Y.; He, M.; Niu, X.; Sun, M. CoMnO_x Nanoflower-Based Smartphone Sensing Platform and Virtual Reality Display for Colorimetric Detection of Ziram and Cu²⁺. *Biosensors* **2024**, *14*, 178.

<https://doi.org/10.3390/bios14040178>

Received: 15 February 2024

Revised: 21 March 2024

Accepted: 4 April 2024

Published: 6 April 2024



Copyright: © 2024 by the authors. Licensee MDPI, Basel, Switzerland. This article is an open access article distributed under the terms and conditions of the Creative Commons Attribution (CC BY) license (<https://creativecommons.org/licenses/by/4.0/>).

Keywords: cobalt manganese oxide; oxidase-like activity; ziram; Cu²⁺; intelligent detection

1. Introduction

Zinc dimethyl dithiocarbamate (ziram) is a widely used organosulfur fungicide that can inhibit and prevent diseases caused by a variety of fungi. However, due to the overuse and abuse of ziram, it often leads to pesticide residues in food and water, causing serious effects on human health. With the increase of living standards, pesticide residue in food has become a hot issue in society, and research on pesticide residue detection has become popular. Currently, common methods for the determination of pesticide residues include high-performance liquid chromatography (HPLC) [1], spectrophotometry [2], capillary electrophoresis [3], and voltammetry [4]. However, all of the above methods are not suitable for in-field analysis, severely constraining the widespread use of the above techniques for detecting pesticide residues on site and in a timely manner. Simple, rapid, and sensitive modes for detecting pesticide residues need to be developed.

Nanozymes are nanomaterials that can catalyze enzyme substrates under mild or extreme conditions and convert the substrates into products following enzyme kinetics. Since the first study of Fe₃O₄ nanomaterials with horseradish peroxidase (HRP) catalytic activity was reported in 2007 [5], great effort has been made to develop nanomaterials with similar catalytic activity [6–9]. Nanozymes present a lower cost, higher stability, higher adaptation to extreme conditions, and higher recovery efficiency than natural enzymes.

In recent years, metals [10,11], metal composites [12–14], and carbon-based materials [15] have all been discovered and designed as nanomaterials with enzyme-like catalytic effects. Nanozymes have been extensively studied in biosensors, environmental protection, disease diagnosis, and antimicrobial agents [16–18]. Among all the various nanozymes, redox nanozymes are the most studied. According to different catalytic types, redox nanozymes often present many kinds of simulated enzyme activities, such as peroxidase- (POD), oxidase- (OXD), catalase- (CAT), and superoxide dismutase-like (SOD) activities [19–22]. Most research in the field currently focuses on peroxidase-like activity, whereas oxidase-like activity receives much less attention [23–26]. In the process of catalysis by peroxidase mimics, external H_2O_2 is required to act as an electron acceptor. For oxidase catalysis, dissolved O_2 can be used as a substrate, so the catalytic operation is more direct and simpler. As a result, oxidase-like nanozymes act as a compelling option for creating sensors with a straight-forward operation, excellent compatibility, and high reliability.

Manganese oxides (MnO_x) have been widely used to detect various small biomolecules based on their oxidase activity, including hydroquinone [27], organophosphorus [28], and ascorbic acid [29]. Manganese oxides exist in more than 30 different natural crystal forms, and these minerals are important constituents of sediments and soils, participating in various natural chemical reactions [30]. However, manganese oxides have poor catalytic performance, and they are difficult to separate after the reaction. To better mimic natural enzymes, the catalytic activity of nanozymes can be designed by tuning size, morphology, composition, surface functional groups, and exposed faces. Heteroatom doping is a good strategy to enhance the activity of nanozymes. Transition metal-doped nanozymes can exhibit higher catalytic activity than pristine materials [31]. These materials show superior catalytic activity to monometallic materials due to electronic structural effects and synergistic effects.

In this study, CoMnO_x with multiple enzyme-like catalytic properties was designed to construct an “on-off-on” sensing platform for ziram and Cu^{2+} . CoMnO_x was prepared by hydrothermal and calcination methods. The oxidase-, catalase-, and laccase-like activities of the obtained CoMnO_x were evaluated, and the reaction kinetics and mechanisms were studied in detail. The substrate TMB could be oxidized to oxTMB by a large amount of O_2^- generated from oxidase-like catalysis. Meanwhile, it was also oxidized directly to the blue product oxTMB via the high redox ability of Co species. Based on the oxidase activity of CoMnO_x , a multifunctional colorimetric sensing platform for ziram and Cu^{2+} was established, which provided wide detection ranges and low detection limits. The combination of the sensing method and a portable smartphone was further made to achieve real-time detection, and the application potential in monitoring ziram and Cu^{2+} in environmental soil and water was also assessed.

2. Materials and Methods

2.1. Preparation of CoMnO_x

$\text{Co}(\text{NO}_3)_2 \cdot 6\text{H}_2\text{O}$ (0.4366 g) and KMnO_4 (0.2371 g) were gradually put into 21 mL of deionized water with strong stirring. After stirring for 10 min, the mixture was autoclaved in a 30 mL autoclave. After autoclaving, the mixture was transferred into an oven and kept for 6 h at 150 °C. After the heated treatment, the formed product was precipitated to obtain solid powders. The collected solid powders were washed several times by deionized water and ethanol, respectively. Lastly, the powders were treated in a vacuum oven for 12 h. After drying, a certain amount of the solid powders was put into a tube furnace and annealed at 450 °C for 30 min under an argon atmosphere. After calcination, the proposed CoMnO_x was obtained.

2.2. Enzyme-Like Activities of CoMnO_x

Firstly, the OXD-like activity of CoMnO_x was investigated with a conventional method. 3,3',5,5'-Tetramethylbenzidine (TMB) was used as a chromogenic substrate to evaluate the OXD-like activity. During tests, 210 μL of TMB (5 mM) and 150 μL of CoMnO_x

(1 mg·mL⁻¹) were mixed with 0.2 M of HAc-NaAc buffer (the total volume was 3 mL, pH 4.5). Afterwards, the mixture was kept in a water bath at 40 °C for 20 min. After that, the mixture solution was used to investigate the absorbance at 652 nm by an ultraviolet-visible (UV-Vis) spectrophotometer.

To verify the CAT-like activity of CoMnO_x, the mixture solution was prepared by mixing Tris-HCl buffer (pH 8.0), 100 µL of CoMnO_x (1 mg·mL⁻¹), and 200 µL of H₂O₂ (20 mM). After the mixture was kept in a water bath at 25 °C for 10 min, the absorbance at 240 nm was obtained by UV-Vis as time went by.

To characterize the laccase-like activity of CoMnO_x, the mixture solution was prepared by mixing 50 mM of MES buffer (pH 7.0), 100 µL of 2,4-DCP (1.0 mg·mL⁻¹), and 4-AP. The volume of the mixture solution was 1.5 mL. Afterwards, a CoMnO_x suspension was introduced and the mixture was incubated for 90 min at 37 °C. Finally, the solution absorbance was obtained by UV-Vis.

2.3. Steady-State Kinetic Study

After condition optimization experiments, the catalytic property and kinetic parameters of CoMnO_x with oxidase-like activity were investigated. Firstly, a series of mixtures were prepared by mixing 0.2 M of HAc-NaAc buffer (pH 4.5) and 150 µL of CoMnO_x (1 mg·mL⁻¹) with different concentrations of TMB. Then, a series of mixtures were kept in a water bath at 40 °C for 20 min. The oxidase-like activity of these mixtures was obtained at 652 nm under optimized conditions by UV-Vis. Based on the Michaelis–Menten equation, K_m and V_{max} were obtained.

$$1/V = (K_m/V_{max})(1/[S]) + 1/V_{max}$$

where K_m is the Michaelis constant, $[S]$ is the substrate concentration, and V_{max} is the maximum reaction velocity.

2.4. Oxidase-Like Reaction Mechanism

Different radical scavengers were employed to investigate reactive oxygen species (ROS) formed during the oxidase-like reaction. The mixture solution was obtained by mixing 100 µL of different concentrations of scavengers, 210 µL of TMB, 150 µL of CoMnO_x, and HAc-NaAc buffer. Hydroxyl radical (·OH), singlet oxygen (¹O₂), and superoxide anion (O₂⁻) were measured by the radical scavengers of isopropyl alcohol (IPA), NaN₃, and 1,4-benzoquinone (PBQ), respectively. Oxygen vacancies were tested by adding EDTA. After incubating, the oxidase-like activity of the mixture was tested at 652 nm.

2.5. Colorimetric Detection of Ziram and Cu²⁺

For the colorimetric detection of ziram, 210 µL of TMB and 150 µL of CoMnO_x were mixed with HAc-NaAc buffer. Then, the effects of various concentrations of ziram on the oxidase-like activity of the mixture were investigated. After incubating, the intensity of absorbance at 652 nm was tested by UV-Vis.

For the colorimetric detection of Cu²⁺, 480 µL of ziram (4 mM) and various Cu²⁺ concentrations were mixed with the HAc-NaAc buffer system containing 210 µL of TMB and 150 µL of CoMnO_x. After incubating at 40 °C, the effects of various concentrations of Cu²⁺ on the absorbance were investigated, and the intensity of absorbance at 652 nm was tested by UV-Vis.

2.6. Visual Smartphone Detection Platform

Based on the colorimetric detection of ziram and Cu²⁺, a portable smartphone platform was established for instant analysis. Firstly, a large number of photos were collected, and then the red-green-blue (RGB) and hue-saturation-lightness (HSL) of the photos were extracted and trained by deep learning. As for the intelligent detection of ziram and Cu²⁺, the photos of colorimetric results were uploaded to a smartphone, and the values of RGB

and HSL could be recognized automatically by an artificial intelligence program. The values or their combinations of RGB/HSL and the concentrations of targets were used to establish standard curves by the smartphone. At the same time, the results of the linear equation and correlation coefficient were formed automatically.

2.7. Real Sample Analysis

To investigate the practicability of the developed sensing platform based on the oxidase-like activity of CoMnO_x , a standard addition method was employed. The supernatants of river water and soil were obtained after centrifugation treatment. Before testing, the obtained liquids were diluted 100 times. Certain concentrations of Cu^{2+} and ziram were added into the liquids. The color photos were taken and uploaded to the smartphone platform. The values of RGB and HSL could be recognized automatically by the artificial intelligence program, and the corresponding concentrations of Cu^{2+} and ziram were output automatically.

3. Results

3.1. Synthesis and Characterization of CoMnO_x Nanoflowers

The synthesis diagram of CoMnO_x is presented in Figure 1A. The samples of CoMnO_x were prepared by hydrothermal synthesis and high-temperature calcination. Figure 1B–E show that the obtained CoMnO_x has a flower-like shape with rich petal wrinkles. The possible mechanism for CoMnO_x forming such a flower-like structure is MnO_x crystal nucleus growth during the Ostwald ripening process [32]. The distribution of elements is displayed in Figure 1F. The results reveal that Co, Mn, and O elements disperse homogeneously. The X-ray diffraction (XRD) pattern of CoMnO_x presents diffraction peaks of (111), (220), and (422) (Figure S1), which are attributed to MnO_x (PDF# 21-0547). As shown in Figure S1, no corresponding Co peak is observed. It is presumed that Co is uniformly doped into MnO_x , and the crystal form of MnO_x is not changed [33]. The corresponding FT-IR spectrum is illustrated in Figure S2, and the peak at 530 cm^{-1} belongs to the stretching vibration of Co–O [34]. The peak at 3412 cm^{-1} is assigned to the O–H stretching vibration of H_2O [35].

X-ray photoelectron spectroscopy (XPS) is used to analyze the elemental content and chemical state of CoMnO_x . The XPS survey spectrum (Figure S3A) shows the elements of Co, Mn, and O observed on CoMnO_x surface. As shown in Figure S3B, the peaks of 641.91 eV and 653.54 eV should be ascribed to Mn $2p_{3/2}$ and Mn $2p_{1/2}$ of Mn^{3+} , and the peaks of 643.10 eV and 654.38 eV are attributed to Mn $2p_{3/2}$ and Mn $2p_{1/2}$ of Mn^{2+} [13,15]. Figure S3C shows that the peaks of 796.94 eV and 782.79 eV are associated with Co $2p_{1/2}$ and $2p_{3/2}$ of Co^{2+} , and the peaks at 795.37 eV and 780.37 eV for Co $2p_{1/2}$ and $2p_{3/2}$ are associated with Co^{3+} [34,35]. The content of $\text{Co}^{3+}/(\text{Co}^{2+}+\text{Co}^{3+})$ is as high as 71.09%, indicating that Co^{3+} is the main species of Co in the obtained CoMnO_x . Thus, the redox ability of CoMnO_x is attributed to the different valence states of Mn and Co elements. The surface O species are displayed in Figure S3D. Three kinds of O species, namely surface lattice oxygen (O_l), oxygen vacancy (O_v), and chemisorbed oxygen (O_{ads}), are presented. O_l , O_v , and O_{ads} are located at 529.85 eV, 531.29 eV, and 532.35 eV, respectively [36]. The O_l species accounts for 72.97% of the total surface oxygen, and O_v and O_{ads} account for 17.15% and 9.88%, respectively.

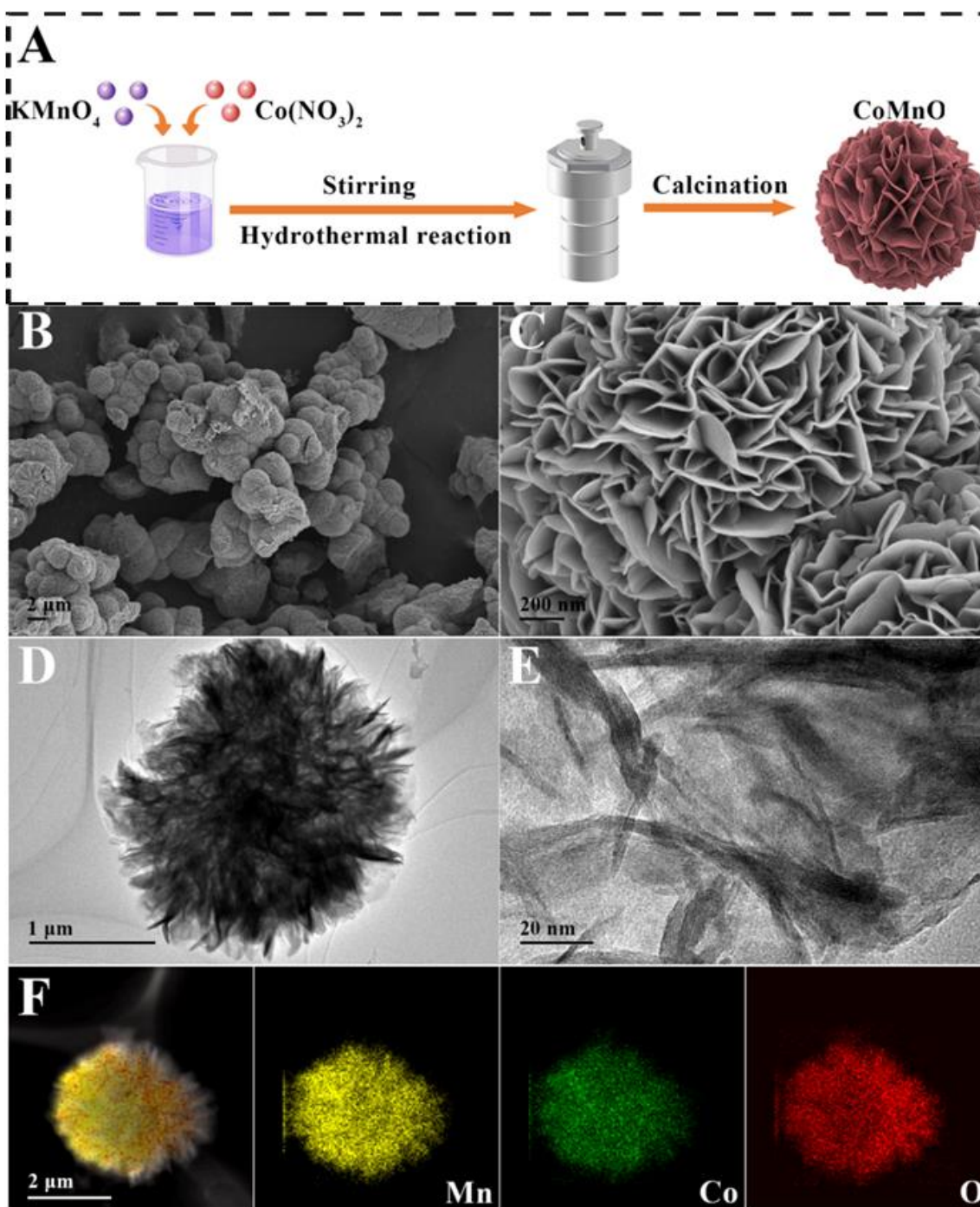


Figure 1. Synthesis and characterization of CoMnO_x nanoflowers. (A) Synthesis diagram; (B,C) scanning electron microscopy (SEM) of CoMnO_x nanoflowers; (D,E) transmission electron microscopy (TEM) of CoMnO_x nanoflowers; (F) elemental mapping pattern of CoMnO_x nanoflowers.

3.2. Enzyme-Like Catalytic Activities and Mechanisms

3.2.1. Enzyme-Like Catalytic Activities

The oxidase-like activity of CoMnO_x was evaluated (shown in Figure 2A). It shows that no absorption peaks at 652 nm are found with only TMB or CoMnO_x in the reaction system. However, a characteristic absorption peak is observed in the presence of $\text{CoMnO}_x + \text{TMB}$, indicating that TMB can be oxidized into oxTMB due to the oxidase-like activity of CoMnO_x . In addition, the condition optimization experiments are displayed in Figure S4. As for the effect of pH on the oxidase-like activity of CoMnO_x , the intensity

of absorbance increases with pH from 2.5 to 4.5, and then it decreases after a pH above 4.5. Thus, the optimal pH is 4.5 (Figure S4A). The effect of temperature on the oxidase-like activity is the same as that of pH, and the highest intensity of absorbance is obtained at 40 °C (Figure S4B). As for the effect of CoMnO_x concentration, the intensity of absorbance increases from 0.01 mg·mL⁻¹ to 0.05 mg·mL⁻¹ and then remains unchanged. Thus, the optimized concentration of CoMnO_x is 0.05 mg·mL⁻¹ (Figure S4C). For the effect of TMB concentration, the intensity of absorbance increases until a TMB concentration of up to 0.35 mM (Figure S4D). Therefore, the highest oxidase-like activity of CoMnO_x is presented at pH 4.5 and 40 °C. Meanwhile, the optimized concentrations of CoMnO_x and TMB are 0.05 mg·mL⁻¹ and 0.35 mM, respectively.

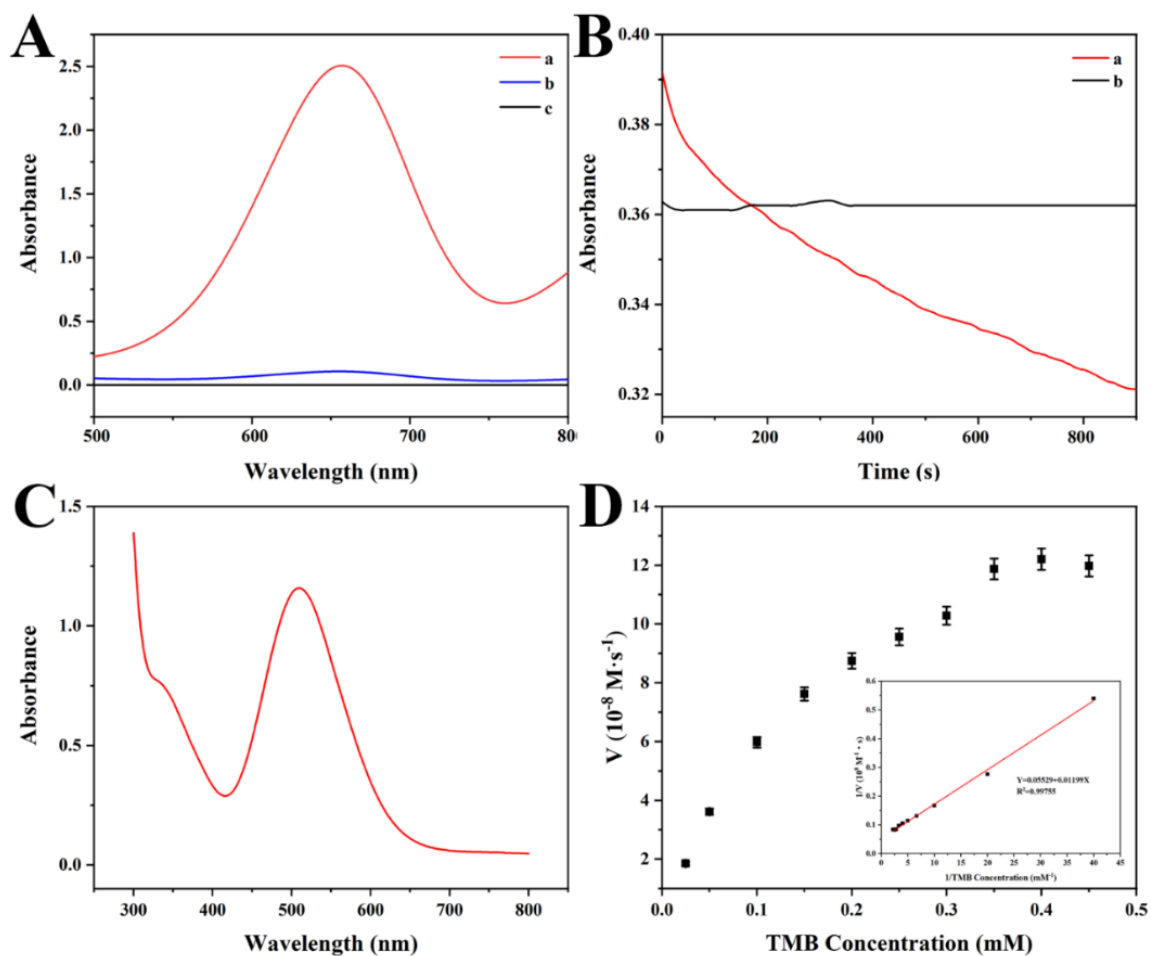


Figure 2. (A) UV-Vis absorbance spectra of different treatments for oxidase-like activity (a: CoMnO_x + TMB, b: TMB, c: CoMnO_x) after incubation at 40 °C and pH 4.5; (B) UV-Vis of different treatments for catalase-like activity (a: CoMnO_x + H₂O₂, b: H₂O₂) after incubation at 40 °C and pH 4.5; (C) UV-Vis of the mixture of CoMnO_x suspension, 50 mM MES buffer (pH 7.0), 100 μL 2,4-DCP (1.0 mg·mL⁻¹), and 4-AP for laccase-like activity after incubation for 90 min at 37 °C; (D) study on the steady-state kinetics of CoMnO_x after incubation at 40 °C for 20 min (Lineweaver-Burk reciprocal plot, *n* = 3).

The catalase-like activity of CoMnO_x was determined by the degradation of H₂O₂. The results show that the intensity of absorbance is not changed with the increase in time when only H₂O₂ exists. This indicates that the H₂O₂ is not degraded. However, the intensity of absorbance decreases as time increases for the CoMnO_x + H₂O₂ system, and bubbles are produced simultaneously, proving that CoMnO_x has catalase-like activity (Figure 2B).

As for the laccase-like activity of CoMnO_x, 2,4-DCP was used as a substrate, and the color of the CoMnO_x + 2,4-DCP + 4-AP system changes from colorless to red. The intensity of absorbance presents an increase first and then a decreasing trend from 400 nm to 600 nm, and a strong UV-Vis absorption peak at 510 nm is observed in Figure 2C. This indicates that CoMnO_x has specific laccase-like activity, which may be applied in the field of biosensing [37].

3.2.2. Kinetic Studies

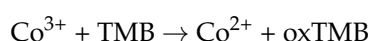
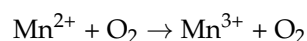
The oxidase-like catalytic efficiency was investigated by steady-state kinetics under optimal conditions [21]. Typical Michaelis–Menten curves were studied under different concentrations of TMB [38]. The typical Lineweaver–Burk equation is $Y = 0.05529 + 0.01199X$. Based on the Lineweaver–Burk equation, the K_m of CoMnO_x is 0.0022 mM and the V_{max} value is 0.1809 $\mu\text{M}\cdot\text{s}^{-1}$ (Figure 2D). Compared to other literature (Table S1), the K_m value of CoMnO_x is lower than that of other nanozymes, indicating that CoMnO_x has stronger affinity toward TMB.

3.2.3. Catalytic Mechanisms

N₂ purging experiments and reactive oxygen species (ROS) scavenging experiments were carried out to investigate the catalytic oxidation mechanism. The role of dissolved oxygen in the catalytic oxidation reaction of CoMnO_x was studied under different atmospheric conditions (O₂, N₂, and air). The absorbance increased under the O₂ atmosphere (Figure 3A). However, the catalytic activity was inhibited under the N₂ atmosphere. This indicates that O₂ plays a key role in the oxidase process of CoMnO_x.

The oxidase-like catalytic processes of CoMnO_x were further determined by changing different scavengers [39]. Different radical scavengers were employed to investigate reactive oxygen species (ROS) formed during the oxidase-like reaction. Ethylenediaminetetraacetic acid (EDTA), isopropanol (IPA), *p*-benzoquinone (PBQ), and sodium azide (NaN₃) were used as scavengers of oxygen vacancy (OV), hydroxyl radical ($\cdot\text{OH}$), superoxide anion (O₂[−]), and singlet oxygen (¹O₂), respectively. The absorbances decreased when increasing the concentration of the scavengers (EDTA, IPA, PBQ, and NaN₃), indicating that the catalytic oxidation of CoMnO_x is related to OV and the other three kinds of ROS (Figure 3B). Compared with the results of other radical scavengers, the absorbance was most severely decreased after PBQ addition. The intensity of absorbance almost dropped to zero when the PBQ was up to 10 mM. The results show that O₂[−] plays the most important role.

Figure 3C–E and Table S2 show that the Co²⁺/Co³⁺ ratio increases from 0.407 to 0.726 during the reaction and, thus, the content of Co²⁺ increases significantly in the CoMnO_x + TMB system. This is because CoMnO_x can catalyze TMB to oxTMB, making an electron transfer from TMB to Co³⁺. The surface Mn²⁺/Mn³⁺ ratio of CoMnO_x slightly increases during catalytic oxidation. According to Table S3, the proportion of oxygen vacancies increases from 17.15% to 26.57% during the catalytic reaction, while the proportion of surface lattice oxygen decreases from 72.97% to 64.17%. The increase of oxygen vacancy during the reaction might optimize the adsorption energy of the reaction substrate on the surface of CoMnO_x. The decrease of surface lattice oxygen indicates that lattice oxygen can take part in the oxidase reaction. O₂ molecules adsorbed on the surface of CoMnO_x are activated to produce a large amount of O₂[−]. Then, O₂[−] can extract acidic hydrogen from TMB to produce the blue product oxTMB. Meanwhile, TMB is adsorbed and oxidized to the blue product oxTMB via Co³⁺, and Co³⁺ is reduced to Co²⁺ via electron transfer. Finally, the CoMnO_x nanozyme is regenerated (Figure 3F). Therefore, reasonable mechanisms for the oxidase-like activity are speculated and presented as follows:



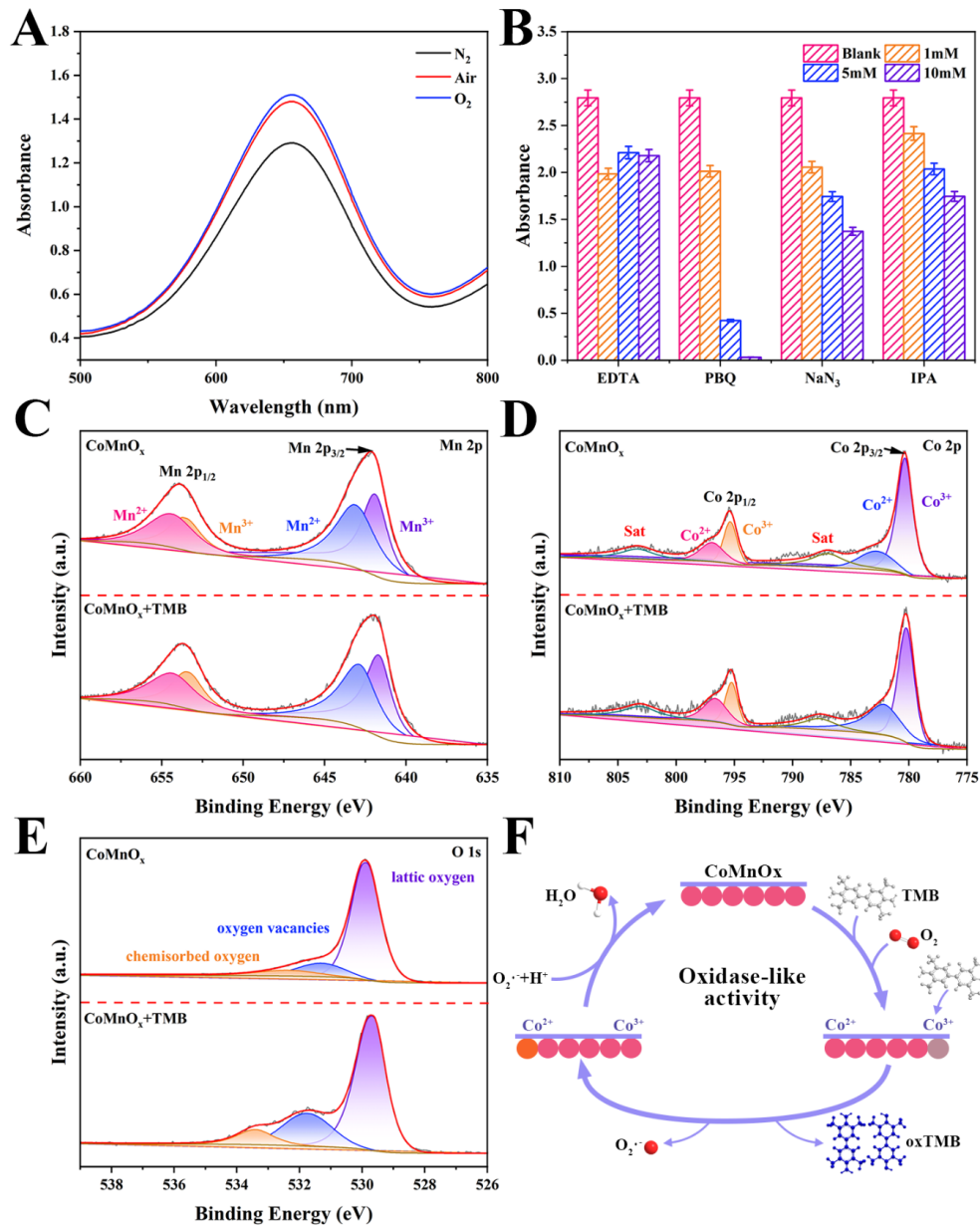
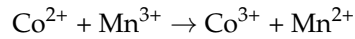


Figure 3. (A) UV-Vis spectra of CoMnO_x + TMB in N₂, air, or O₂-saturated systems after incubation at 40 °C and pH 4.5; (B) relative activity of different scavengers in the CoMnO_x + TMB system ($n = 3$); (C–E) XPS characterization: (C) Mn 2p, (D) Co 2p, (E) O 1s; (F) possible mechanism of CoMnO_x showing oxidase-like activity.

3.3. Colorimetric Sensing

Colorimetric methods for the analysis of ziram and Cu²⁺ were further established using the oxidase activity of CoMnO_x. Compared with the absorbance of the TMB + CoMnO_x system, the absorbance at 652 nm decreases slowly with the increasing concentration of ziram in the range of 5~280 μM (Figure 4A). Figure 4B reveals that the linear relationship is $Y = 0.0054 + 8.7715X$ ($R^2 = 0.9902$). According to the LOD equation ($3\delta/S$, where δ is the standard deviation of the blank solution and S is the slope of the calibration curve), the LOD of ziram is 1.475 μM. These results reveal that the sensing platform for ziram has a wider linear range compared to the previous reports listed in Table S4. Figure 4C

shows that the absorbance of $\text{CoMnO}_x + \text{TMB} + \text{ziram} + \text{Cu}^{2+}$ gradually increases with the increase of Cu^{2+} content. The UV absorbance of the reaction system can be restored by adding Cu^{2+} , which indicates that the interaction of ziram and Cu^{2+} may exist. Figure 4D shows that the linear range is 80–360 μM and the linear relationship is $Y = 0.8510 + 5.3318X$ ($R^2 = 0.9876$). In comparison with the other studies shown in Table S5, the detection range of Cu^{2+} is relatively wide.

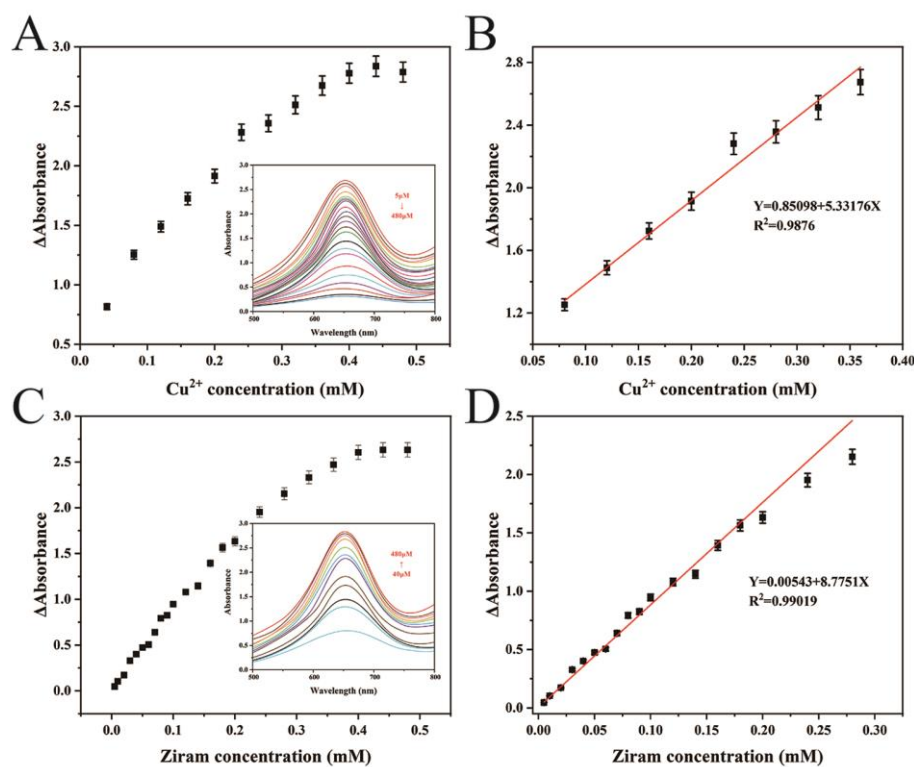


Figure 4. (A) Effects of various concentrations of ziram on the oxidase-like activity of the mixture of 210 μL TMB, 150 μL CoMnO_x , and HAc-NaAc buffer at 652 nm ($n = 3$); (B) corresponding calibration curve of ziram; (C) effects of various concentrations of Cu^{2+} on the oxidase-like activity of the mixture of 480 μL ziram (4 mM), 210 μL TMB, 150 μL CoMnO_x , and HAc-NaAc buffer at 652 nm ($n = 3$); (D) corresponding calibration curve of Cu^{2+} .

3.4. Detection Mechanisms

In order to explain the detection mechanism clearly, the detection processes of ziram and Cu^{2+} are revealed by virtual reality (VR) technology. A three-dimensional spatial model of the detailed reaction process is established using a computer system (Figure 5A). The user can wear VR glasses to observe and experience the specific detection process (Figure 5B). Figure 5C displays the detail detection mechanism. Firstly, O_2 is adsorbed on the active sites of CoMnO_x (I). Secondly, O_2 is catalyzed by CoMnO_x to produce O_2^- due to the electron transfer of Co and Mn elements (II). Thirdly, TMB is oxidized by O_2^- to form oxTMB. Meanwhile, the color is changed from colorless to blue (III). Fourthly, the interaction between ziram and oxTMB is formed, and the color is returned to colorless after adding ziram (IV and V). According to the structure of ziram (Figure S5), the negative charge center N atom of ziram can produce an interaction with the oxTMB cationic radicals. At the same time, the two strong electron-donating methyl groups of ziram and the electronegative center of N atom, can transfer the electron to oxTMB and make the blue color lighter. Moreover, the produced O_2^- cannot oxidize the reduced oxTMB due to the interaction between ziram and oxTMB. Fifthly, the coordination effect of Cu^{2+} and ziram can get rid of the interaction of ziram and oxTMB, making the color return to the blue. Moreover, the

detection mechanisms of ziram and Cu^{2+} based on CoMnO_x are also revealed in Figure 5D and the supporting video.

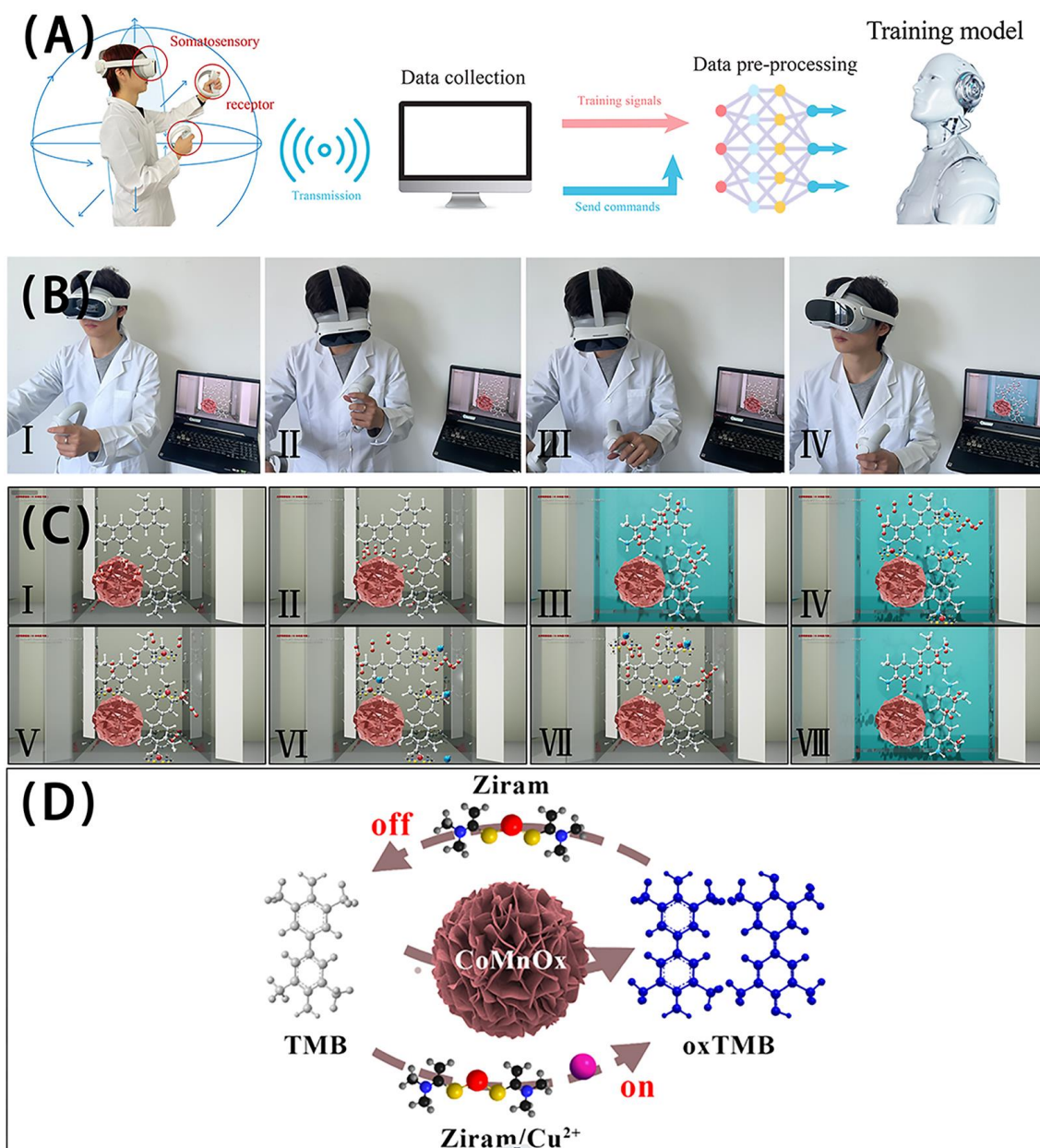


Figure 5. (A) Flow chart of virtual space establishment and design; (B) interactive experience of virtual reality design; (C) key training items in the virtual reality space. Step I: O_2 adsorption; II: O_2^- production; III: TMB oxidation by O_2^- ; IV and V: interaction of ziram and oxTMB; VI: inhibitory effect of TMB oxidation by O_2^- after adding ziram; VII: interaction of Cu^{2+} and ziram; VIII: recovery of oxidase-like activity; (D) detection mechanisms of ziram and Cu^{2+} based on CoMnO_x .

3.5. Smartphone Platform for Target Analysis

The object detection model is established based on the object recognition and positioning algorithm of deep learning. The colors of the cuvette photos are automatically extracted and classified by the model, and the corresponding Red-Green-Blue (RGB) or Hue-Saturation-Value (HSV) values are calculated. Users only need to input the corresponding concentrations of detected objects and the number of samples, and the target linear curves of RGB or HSV values and the concentrations of detected objects are fitted automatically.

As shown in Figure 6, the blue color becomes lighter and brighter when ziram is added into the system. The photos of the colorimetric results are uploaded to the smartphone, and the values of RGB and HSV can be recognized automatically by the artificial intelligence program. Compared with other fitting results, the H value and ziram concentration are used for linear fitting due to the highest correlation coefficient. Finally, the linear equation of $Y = 203.7802 - 0.1237X$ ($R^2 = 0.9923$) is generated automatically (Figure 6A), which can be used for on-site and timely ziram detection. Similarly, the smartphone can also detect the concentration of Cu^{2+} . Compared with other fitting results, the G value and Cu^{2+} concentration present the highest correlation coefficient. The linear equation of $Y = 152.6481 - 0.6496X$ ($R^2 = 0.9915$) is obtained for Cu^{2+} detection (Figure 6B).



Figure 6. Intelligent detection platform for (A) ziram and (B) Cu^{2+} .

3.6. Real Sample Analysis

Environmental samples of ziram and Cu^{2+} are simulated by the standard addition method to prove the practicability of the platform. Compared with the standard values of ziram, the recovery ranges from 96.60% to 102.18%, and the relative standard deviations (RSD) range from 1.04% to 3.67% ($n = 3$) (Table S6). As for Cu^{2+} detection (Table S7), the recovery is between 98.73% and 100.42%, and the RSD ranges from 0.52% to 4.69% ($n = 3$). These results confirm the applicability of the intelligent platform in real sample detection.

3.7. Selectivity and Stability Assay

Interfering pesticide substances of 2,4-dichlorophenoxyacetic acid, glufosinate ammonium, ethrel, carbendazim, acetamiprid, and atrazine are measured based on the detection platform (Figure S6A). In addition, the concentrations of these species are 100 times higher than that of ziram. The absorbance of each interfering substance is unchanged compared to the blank, except ziram. These results indicate that CoMnO_x has excellent specificity for ziram detection. To evaluate Cu^{2+} sensing selectivity, Na^+ , Mn^{2+} , Mg^{2+} , Zn^{2+} , Ca^{2+} , K^+ , Al^{3+} , Pb^{2+} , and Cd^{2+} (their concentrations are 100 times higher than that of Cu^{2+}) are used as interfering substances (Figure S6B). In comparison with other metal ions, only the combination of Cu^{2+} and ziram can restore the absorption. These results show that the sensor has a high selectivity for Cu^{2+} detection.

The stability and reproducibility of the oxidase activity of CoMnO_x were also tested. As shown in Figure S5C, CoMnO_x can maintain high activity even after 60 days, indicating that CoMnO_x has good stability. In addition, 10 batches of CoMnO_x nanoflowers are synthesized repeatedly and their enzyme activities are measured (Figure S6D). The results show that the relative standard deviation (RSD) of different batches of CoMnO_x nanoflowers is only 3.19%, which indicates that CoMnO_x has good reproducibility (Figure S6D).

4. Discussion

The CoMnO_x nanozyme is designed and synthesized by hydrothermal reaction and high-temperature calcination methods. The obtained flower-shaped CoMnO_x presents three kinds of nanozyme activities, namely oxidase-, catalase-, and laccase-like activities. Among them, the oxidase-like activity is studied in detail. In addition, the highest oxidase-like activity of CoMnO_x is presented at a pH of 4.5 and temperature of 40 °C. Moreover, the oxidase-like catalytic efficiency was investigated by steady-state kinetics under optimal conditions. The V_{\max} value is 0.1809 $\mu\text{M}\cdot\text{s}^{-1}$ and the K_m of CoMnO_x is 0.0022 mM, which is much lower than that of other nanozymes due to their stronger affinity toward TMB. The high oxidase-like activity is attributed to the changed valence state of Co and Mn elements. During the reaction, the $\text{Co}^{2+}/\text{Co}^{3+}$ ratio increases from 0.407 to 0.726 and the surface $\text{Mn}^{2+}/\text{Mn}^{3+}$ ratio of CoMnO_x is also slightly increased. Moreover, the proportion of oxygen vacancies increases from 17.15% to 26.57% during the catalytic reaction, while the proportion of surface lattice oxygen decreases from 72.97% to 64.17%. In detail, O_2 molecules adsorbed on the surface of CoMnO_x are activated to produce a large amount of ROS ($\cdot\text{OH}$, O_2^- , and 1 O_2), especially O_2^- . According to the changes of oxygen species, some lattice oxygen can take part in the oxidase reaction to produce O_2^- , and lattice oxygen is changed to oxygen vacancies. O_2^- can extract acidic hydrogen from TMB to produce the blue product oxTMB. Meanwhile, TMB is adsorbed and oxidized to the blue product oxTMB via Co^{3+} , and Co^{3+} is reduced to Co^{2+} via electron transfer. CoMnO_x , as an oxidase-like catalyst, can remain unchanged after the reaction. In other words, the nanozyme is regenerated after the reaction.

Based on its excellent oxidase activity, an “on-off-on” colorimetric sensor for the detection of ziram and Cu^{2+} has been developed. The absorbance at 652 nm decreases slowly after adding ziram. The reason might be that the active sites of CoMnO_x are covered by ziram. However, the absorbance of the $\text{CoMnO}_x + \text{TMB} + \text{ziram}$ is restored gradually after the addition of Cu^{2+} , indicating that the active sites of CoMnO_x are uncovered due to the interaction of ziram and Cu^{2+} . The linear detection ranges for ziram and Cu^{2+} are

5~280 μM and 80~360 μM , and the detection limits are 1.475 μM and 3.906 μM , respectively. The detection of ziram shows wider detection ranges and lower detection limits than that in other studies (Table S4), and the detection of Cu^{2+} also shows a relatively wide detection range compared with other studies (Table S5). Moreover, an intelligent detection platform has further been established by combining the colorimetric signals with a portable smartphone. The developed ziram and Cu^{2+} portable smartphone platform can be used in environment analysis instantaneously.

5. Conclusions

In summary, flower-like CoMnO_x has been successfully synthesized by hydrothermal synthesis and high temperature calcination. The obtained CoMnO_x presents OXD-, CAT-, and laccase-like activities. The reaction kinetics and mechanisms have been studied deeply. The reaction kinetic results show that CoMnO_x has a strong affinity toward TMB with a low K_m (0.0022 mM). The reaction mechanisms show that TMB can be oxidized to oxTMB by a large amount of generated O_2^- . Meanwhile, TMB is also oxidized directly to the blue product oxTMB via the high redox ability of Co species. Based on its excellent oxidase activity, an “on-off-on” colorimetric sensor for the detection of ziram and Cu^{2+} has been developed. The linear detection ranges for ziram and Cu^{2+} are 5~280 μM and 80~360 μM , and the detection limits are 1.475 μM and 3.906 μM , respectively. The detection of ziram and Cu^{2+} shows wider detection ranges and lower limits than that in other studies. Moreover, a ziram and Cu^{2+} portable smartphone platform has been constructed successfully and used in on-site and timely environment analysis.

Supplementary Materials: The following supporting information can be downloaded at: <https://www.mdpi.com/article/10.3390/bios14040178/s1>, Figure S1: XRD image of CoMnO_x ; Figure S2: FTIR spectrum of CoMnO_x ; Figure S3: (A–D) XPS full, (B) Mn 2p, (C) Co 2p, and (D) O 1s spectra of CoMnO_x ; Figure S4: Optimization of reaction conditions based on CoMnO_x oxidase-like activity: (A) pH; (B) temperature; (C) material concentration; (D) TMB concentration ($n = 3$); Figure S5: Potential interference of other substances for the detection of (A) ziram and (B) Cu^{2+} ; (C and D) stability and reproducibility of the nanozyme for target sensing; Table S1: Comparison of steady-state kinetic parameters for the oxidase-like activity of CoMnO_x and other nanozymes; Table S2: XPS analysis results of Mn 2p and Co 2p; Table S3: XPS analysis results of O 1s; Table S4: Comparison of different methods for the detection of ziram; Table S5: Comparison of different methods for the detection of Cu^{2+} ; Table S6: Assay results of ziram in soil and water samples; Table S7: Assay results of Cu^{2+} in soil and water samples. [40–66].

Author Contributions: Conceptualization, F.W., M.H. and M.S.; methodology, C.S., X.Z. and Y.M.; software, C.S. and Y.M.; validation, C.S. and X.Z.; formal analysis, M.H.; investigation, C.S., F.W. and Y.W.; resources, X.N. and M.S.; data curation, F.W. and Y.W.; writing—original draft preparation, F.W.; writing—review and editing, X.N. and M.S.; visualization, C.S.; supervision, X.N.; project administration, X.N. and M.S.; funding acquisition, X.N. and M.S. All authors have read and agreed to the published version of the manuscript.

Funding: The authors thank the National Natural Science Foundation of China (Grant No. 32302773), Natural Science Foundation of Sichuan Province (Grant No. 2022NSFSC0227 and 2023NSFSC0618), and National Training Program of Innovation and Entrepreneurship for Undergraduates (Grant No. S202310555038).

Institutional Review Board Statement: Not applicable.

Informed Consent Statement: Not applicable.

Data Availability Statement: The data presented in this study are available in Supplementary Materials.

Conflicts of Interest: The authors declare no conflict of interest.

References

1. Čuš, F.; Česnik, H.B.; Bolta, Š.V. Pesticide residues, copper and biogenic amines in conventional and organic wines. *Food Control* **2022**, *132*, 108534. [[CrossRef](#)]
2. Zhang, C.; Qiu, M.; Wang, J.; Liu, Y. Recent advances in nanoparticle-based optical sensors for detection of pesticide residues in soil. *Biosensors* **2023**, *13*, 415. [[CrossRef](#)] [[PubMed](#)]
3. Auer, F.; Guttman, A. Size separation of sodium dodecyl sulfate-proteins by capillary electrophoresis in dilute and ultra-dilute dextran solutions. *Electrophoresis* **2023**, *44*, 1607–1614. [[CrossRef](#)] [[PubMed](#)]
4. Wei, X.-P.; Luo, Y.-L.; Xu, F.; Chen, Y.-S.; Yang, L.-H. In-situ non-covalent dressing of multi-walled carbon nanotubes@titanium dioxides with carboxymethyl chitosan nanocomposite electrochemical sensors for detection of pesticide residues. *Mater. Design* **2016**, *111*, 445–452. [[CrossRef](#)]
5. Gao, L.; Zhuang, J.; Nie, L.; Zhang, J.; Zhang, Y.; Gu, N.; Wang, T.; Feng, J.; Yang, D.; Perrett, S.; et al. Intrinsic peroxidase-like activity of ferromagnetic nanoparticles. *Nat. Nanotechnol.* **2007**, *2*, 577–583. [[CrossRef](#)] [[PubMed](#)]
6. Wu, J.; Wang, X.; Wang, Q.; Lou, Z.; Li, S.; Zhu, Y.; Qin, L.; Wei, H. Nanomaterials with enzyme-like characteristics (nanozymes): Next-generation artificial enzymes (II). *Chem. Soc. Rev.* **2019**, *48*, 1004–1076. [[CrossRef](#)] [[PubMed](#)]
7. Fang, G.; Kang, R.; Cai, S.; Ge, C. Insight into nanozymes for their environmental applications as antimicrobial and antifouling agents: Progress, challenges and prospects. *Nano Today* **2023**, *48*, 101755. [[CrossRef](#)]
8. Su, L.; Qin, S.; Xie, Z.; Wang, L.; Khan, K.; Tareen, A.K.; Li, D.; Zhang, H. Multi-enzyme activity nanozymes for biosensing and disease treatment. *Coordin. Chem. Rev.* **2022**, *473*, 214784. [[CrossRef](#)]
9. Huang, Y.; Ren, J.; Qu, X. Nanozymes: Classification, catalytic mechanisms, activity regulation, and applications. *Chem. Rev.* **2019**, *119*, 4357–4412. [[CrossRef](#)] [[PubMed](#)]
10. Huang, H.; Lei, L.; Bai, J.; Zhang, L.; Song, D.; Zhao, J.; Li, J.; Li, Y. Efficient elimination and detection of phenolic compounds in juice using laccase mimicking nanozymes. *Chin. J. Chem. Eng.* **2021**, *29*, 167–175. [[CrossRef](#)]
11. Huang, S.; Chen, X.; Lei, Y.; Zhao, W.; Yan, J.; Sun, J. Ionic liquid enhanced fabrication of small-size BSA-Cu laccase mimicking nanozymes for efficient degradation of phenolic compounds. *J. Mol. Liq.* **2022**, *368*, 120197. [[CrossRef](#)]
12. Zhu, J.; Cui, Q.; Wen, W.; Zhang, X.; Wang, S. Cu/CuO-graphene foam with laccase-like activity for identification of phenolic compounds and detection of epinephrine. *Chem. Res. Chin. Univ.* **2022**, *38*, 919–927. [[CrossRef](#)]
13. Facure, M.H.M.; Andre, R.S.; Cardoso, R.M.; Mercante, L.A.; Correa, D.S. Electrochemical and optical dual-mode detection of phenolic compounds using MnO₂/GQD nanozyme. *Electrochim. Acta* **2023**, *441*, 141777. [[CrossRef](#)]
14. Liang, S.; Wu, X.-L.; Xiong, J.; Yuan, X.; Liu, S.-L.; Zong, M.-H.; Lou, W.-Y. Multivalent Ce-MOFs as biomimetic laccase nanozyme for environmental remediation. *Chem. Eng. J.* **2022**, *450*, 138220. [[CrossRef](#)]
15. Ge, H.; Zhang, H. Fungus-based MnO/porous carbon nanohybrid as efficient laccase mimic for oxygen reduction catalysis and hydroquinone detection. *Nanomaterials* **2022**, *12*, 1596. [[CrossRef](#)] [[PubMed](#)]
16. Cheng, Y.; Xia, Y.-D.; Sun, Y.-Q.; Wang, Y.; Yin, X.-B. “Three-in-one” nanozyme composite for augmented cascade catalytic tumor therapy. *Adv. Mater.* **2023**, *36*, 2308033. [[CrossRef](#)] [[PubMed](#)]
17. Ke, C.; Wu, Y.; Song, Z.; Zheng, M.; Zhu, H.; Guo, H.; Sun, H.; Liu, M. A novel competitive fluorescence colorimetric dual-mode immunosensor for detecting ochratoxin A based on the synergistically enhanced peroxidase-like activity of AuAg NCs-SPCN nanocomposite. *Food Chem.* **2024**, *437*, 137930. [[CrossRef](#)] [[PubMed](#)]
18. Cui, Y.; Zhang, W.; Shan, J.; He, J.; Niu, Q.; Zhu, C.; Wang, W.; Chen, X.-L.; Wang, X. Copper nanodots-based hybrid hydrogels with multiple enzyme activities for acute and infected wound repair. *Adv. Healthc. Mater.* **2023**, *13*, 2302566. [[CrossRef](#)] [[PubMed](#)]
19. Hamed, E.M.; Rai, V.; Li, S.F.Y. Single-atom nanozymes with peroxidase-like activity: A review. *Chemosphere* **2024**, *346*, 140557. [[CrossRef](#)]
20. Wu, Y.; Chen, W.; Wang, C.; Xing, D. Overview of nanozymes with phosphatase-like activity. *Biosens. Bioelectron.* **2023**, *237*, 115470. [[CrossRef](#)] [[PubMed](#)]
21. Li, Y.; Dong, Y.; Wang, R. Biomimetic electrochemical sensor based on single-atom nickel laccase nanoenzyme for quercetin detection. *Anal. Chem.* **2024**, *96*, 2610–2619. [[CrossRef](#)] [[PubMed](#)]
22. Zandieh, M.; Liu, J. Nanozymes: Definition, activity, and mechanisms. *Adv. Mater.* **2023**, *36*, 2211041. [[CrossRef](#)] [[PubMed](#)]
23. Sheng, J.; Wu, Y.; Ding, H.; Feng, K.; Shen, Y.; Zhang, Y.; Gu, N. Multienzyme-like nanozymes: Regulation, rational design, and application. *Adv. Mater.* **2023**, *36*, 2211210. [[CrossRef](#)] [[PubMed](#)]
24. Diao, Q.; Chen, X.; Tang, Z.; Li, S.; Tian, Q.; Bu, Z.; Liu, H.; Liu, J.; Niu, X. Nanozymes: Powerful catalytic materials for environmental pollutant detection and degradation. *Environ. Sci. Nano* **2024**, *11*, 766–796. [[CrossRef](#)]
25. Liang, H.; Chen, X.; Bu, Z.; Bai, Q.; Liu, J.; Tian, Q.; Tang, Z.; Li, S.; Diao, Q.; Niu, X. When nanozymes meet deoxyribonucleic acid: Understanding their interactions and biomedical diagnosis applications. *Interdiscip. Med.* **2024**, e20230057. [[CrossRef](#)]
26. Li, X.; Ding, S.; Lyu, Z.; Tieu, P.; Wang, M.; Feng, Z.; Pan, X.; Zhou, Y.; Niu, X.; Du, D.; et al. Single-atomic iron doped carbon dots with both photoluminescence and oxidase-like activity. *Small* **2022**, *18*, 2203001. [[CrossRef](#)] [[PubMed](#)]
27. Zhang, B.; Wang, X.; Hu, W.; Liao, Y.; He, Y.; Dong, B.; Zhao, M.; Ma, Y. SPR-enhanced Au@Fe₃O₄ nanozyme for the detection of hydroquinone. *Chemosensors* **2023**, *11*, 392. [[CrossRef](#)]
28. Wang, X.; Sun, Q.; Yu, J.; Sun, J.; Niu, N.; Chen, L. Lignin-based iron single-atom nanozyme for detection of organophosphorus in soil. *Microchem. J.* **2023**, *195*, 109381. [[CrossRef](#)]

29. Lin, J.; Wang, Q.; Wang, X.; Zhu, Y.; Zhou, X.; Wei, H. Gold alloy-based nanozyme sensor arrays for biothiol detection. *Analyst* **2020**, *145*, 3916–3921. [[CrossRef](#)]
30. Lai, W.; Wei, Q.; Xu, M.; Zhuang, J.; Tang, D. Enzyme-controlled dissolution of MnO₂ nanoflakes with enzyme cascade amplification for colorimetric immunoassay. *Biosens. Bioelectron.* **2017**, *89*, 645–651. [[CrossRef](#)] [[PubMed](#)]
31. Zhang, S.; Ruan, H.; Xin, Q.; Mu, X.; Wang, H.; Zhang, X.-D. Modulation of the biocatalytic activity and selectivity of CeO₂ nanozymes via atomic doping engineering. *Nanoscale* **2023**, *15*, 4408–4419. [[CrossRef](#)] [[PubMed](#)]
32. Sorouri, F.; Gholibegloo, E.; Mortezaadeh, T.; Kiani, S.; Foroumadi, A.; Firoozpour, L.; Khoobi, M. Tannic acid-mediated synthesis of flower-like mesoporous MnO₂ nanostructures as T1-T2 dual-modal MRI contrast agents and dual-enzyme mimetic agents. *Sci. Rep.* **2023**, *13*, 14606. [[CrossRef](#)]
33. Liu, W.; Chu, L.; Zhang, C.; Ni, P.; Jiang, Y.; Wang, B.; Lu, Y.; Chen, C. Hemin-assisted synthesis of peroxidase-like Fe-N-C nanozymes for detection of ascorbic acid-generating bio-enzymes. *Chem. Eng. J.* **2021**, *415*, 128876. [[CrossRef](#)]
34. Fan, S.; Zhao, M.; Ding, L.; Li, H.; Chen, S. Preparation of Co₃O₄/crumpled graphene microsphere as peroxidase mimetic for colorimetric assay of ascorbic acid. *Biosens. Bioelectron.* **2017**, *89*, 846–852. [[CrossRef](#)] [[PubMed](#)]
35. Xi, W.; Shen, M.; Yin, X. Molten-salt confined synthesis of nitrogen-doped carbon nanosheets supported Co₃O₄ nanoparticles as a superior oxygen electrocatalyst for rechargeable Zn-air battery. *J. Power Sources* **2023**, *560*, 232692. [[CrossRef](#)]
36. Zhang, J.; Yang, Y.; Qin, F.; Hu, T.; Zhao, X.; Zhao, S.; Cao, Y.; Gao, Z.; Zhou, Z.; Liang, R.; et al. Catalyzing generation and stabilization of oxygen vacancies on CeO_{2-x} nanorods by Pt nanoclusters as nanozymes for catalytic therapy. *Adv. Healthc. Mater.* **2023**, *12*, 2302056. [[CrossRef](#)] [[PubMed](#)]
37. Castrovilli, M.C.; Tempesta, E.; Cartoni, A.; Plescia, P.; Bolognesi, P.; Chiarinelli, J.; Calandra, P.; Cicco, N.; Verrastro, M.F.; Centonze, D.; et al. Fabrication of a new, low-cost, and environment-friendly laccase-based biosensor by electrospray immobilization with unprecedented reuse and storage performances. *ACS Sustainable Chem. Eng.* **2022**, *10*, 1888–1898. [[CrossRef](#)] [[PubMed](#)]
38. Liu, J.; Yang, D.; Hu, W.; Huang, N.; Rong, Y. Piezoelectric BaTiO₃ nanoparticles as oxidase mimics breaking pH limitation for colorimetric detection of glutathione reductase. *Chem. Eng. J.* **2024**, *481*, 148609. [[CrossRef](#)]
39. Liu, Y.; Cheng, Y.; Zhang, H.; Zhou, M.; Yu, Y.; Lin, S.; Jiang, B.; Zhao, X.; Miao, L.; Wei, C.-W.; et al. Integrated cascade nanozyme catalyzes in vivo ROS scavenging for anti-inflammatory therapy. *Sci. Adv.* **2020**, *6*, 2695. [[CrossRef](#)] [[PubMed](#)]
40. Liu, X.; Yan, L.; Ren, H.; Cai, Y.; Liu, C.; Zeng, L.; Liu, A. Facile synthesis of magnetic hierarchical flower-like Co₃O₄ spheres: Mechanism, excellent tetra-enzyme mimics and their colorimetric biosensing applications. *Biosens. Bioelectron.* **2020**, *165*, 112342. [[CrossRef](#)] [[PubMed](#)]
41. Qin, W.; Li, S.; Yang, C.; Ma, Y.; Zhang, H.; Chen, X. Colorimetric detection of sulfite in foods by a TMB-O₂-Co₃O₄ nanoparticles detection system. *J. Agric. Food Chem.* **2014**, *62*, 5827–5834. [[CrossRef](#)] [[PubMed](#)]
42. Zhao, J.; Xie, Y.; Yuan, W.; Li, D.; Liu, S.; Zheng, B.; Hou, W. A hierarchical Co-Fe LDH rope-like nanostructure: Facile preparation from hexagonal lyotropic liquid crystals and intrinsic oxidase-like catalytic activity. *J. Mater. Chem. B* **2013**, *1*, 1263–1269. [[CrossRef](#)] [[PubMed](#)]
43. Xie, J.; Cao, H.; Jiang, H.; Chen, Y.; Shi, W.; Zheng, H.; Huang, Y. Co₃O₄-reduced graphene oxide nanocomposite as an effective peroxidase mimetic and its application in visual biosensing of glucose. *Anal. Chim. Acta* **2013**, *796*, 92–100. [[CrossRef](#)] [[PubMed](#)]
44. Wan, Y.; Qi, P.; Zhang, D.; Wu, J.; Wang, Y. Manganese oxide nanowire-mediated enzyme-linked immunosorbent assay. *Biosens. Bioelectron.* **2012**, *33*, 69–74. [[CrossRef](#)]
45. Sun, M.; He, M.; Jiang, S.; Wang, Y.; Wang, X.; Liu, T.; Song, C.; Wang, S.; Rao, H.; Lu, Z. Multi-enzyme activity of three layers FeO_x@ZnMnFeO_y@Fe-Mn organogel for colorimetric detection of antioxidants and norfloxacin with smartphone. *Chem. Eng. J.* **2021**, *425*, 131823. [[CrossRef](#)]
46. Yang, H.; Yang, R.; Zhang, P.; Qin, Y.; Chen, T.; Ye, F. A bimetallic (Co/2Fe) metal-organic framework with oxidase and peroxidase mimicking activity for colorimetric detection of hydrogen peroxide. *Microchim. Acta* **2017**, *184*, 4629–4635. [[CrossRef](#)]
47. Wang, Y.; Zhu, X.; Ding, F.; Liu, Y.; Yang, L.; Zou, P.; Zhao, Q.; Wang, X. Colorimetric detection of gallic acid based on the enhanced oxidase-like activity of floral-like magnetic Fe₃O₄@MnO₂. *Luminescence* **2018**, *34*, 55–63. [[CrossRef](#)] [[PubMed](#)]
48. Wu, T.; Ma, Z.; Li, P.; Liu, M.; Liu, X.; Li, H.; Zhang, Y.; Yao, S. Colorimetric detection of ascorbic acid and alkaline phosphatase activity based on the novel oxidase mimetic of Fe-Co bimetallic alloy encapsulated porous carbon nanocages. *Talanta* **2019**, *202*, 354–361. [[CrossRef](#)] [[PubMed](#)]
49. Gao, M.; Lu, X.; Nie, G.; Chi, M.; Wang, C. Hierarchical CNFs/MnCo₂O_{4.5} nanofibers as a highly active oxidase mimetic and its application in biosensing. *Nanotechnology* **2017**, *28*, 485708. [[CrossRef](#)] [[PubMed](#)]
50. Silva, L.; Souza, D. Ziram herbicide determination using a polished silver solid amalgam electrode. *Electrochim. Acta* **2017**, *224*, 541–550. [[CrossRef](#)]
51. Chen, Y.; Sun, X.; Wang, X.; Pan, W.; Yu, G.; Wang, J. Carbon dots with red emission for bioimaging of fungal cells and detecting Hg²⁺ and Ziram in aqueous solution. *Spectrochim. Acta A Mol. Biomol. Spectrosc.* **2020**, *233*, 118230. [[CrossRef](#)] [[PubMed](#)]
52. Chen, S.; Huang, M.; Huang, M.; Feng, L. Fluorometric determination of Ziram using CsPbBr₃ quantum dots. *Microchim. Acta* **2021**, *188*, 1–9. [[CrossRef](#)]
53. Hussain, N.; Pu, H.; Abid, H.; Sun, D. Rapid detection of Ziram residues in apple and pear fruits by SERS based on octanethiol functionalized bimetallic core-shell nanoparticles. *Spectrochim. Acta A Mol. Biomol. Spectrosc.* **2020**, *236*, 118357. [[CrossRef](#)] [[PubMed](#)]

54. Ghoto, S.; Khuhawar, M.; Jahangir, T. Silver nanoparticles with sodium dodecyl sulfate as colorimetric probe for detection of dithiocarbamate pesticides in environmental samples. *Anal. Sci.* **2019**, *35*, 631–637. [[CrossRef](#)] [[PubMed](#)]
55. Sun, M.; Huang, S.; Su, G.; Wang, X.; Lu, Z.; Wang, Y.; Liu, T.; Jiang, Y.; Song, C.; Rao, H. Synthesis of pH-switchable Pt/Co₃O₄ nanoflowers: Catalytic mechanism, four-enzyme activity and smartphone biosensing applications. *Chem. Eng. J.* **2022**, *437*, 134414. [[CrossRef](#)]
56. Jiang, X.; Liu, W.; Luo, B.; Liu, X.; Huang, Y.; Wang, D.; Fan, M.; Gong, Z. Copper foam in situ loaded with precious metal nanoparticles as transmission SEIRAS substrate for rapid detection of dithiocarbamate pesticides. *Anal. Methods* **2020**, *12*, 3600–3607. [[CrossRef](#)] [[PubMed](#)]
57. Lafleur, J.; Senkbeil, S.; Jensen, T.; Kutter, J. Gold nanoparticle-based optical microfluidic sensors for analysis of environmental pollutants. *Lab Chip* **2012**, *12*, 4583–4930. [[CrossRef](#)] [[PubMed](#)]
58. Zhong, C.; Qiu, J.; Liu, M.; Yuan, Y.; Zhu, H.; Gao, Y. Rational design and bioimaging application of cholesterol conjugated fluorescence probe for Cu²⁺ detection. *J. Photochem.* **2021**, *414*, 113267. [[CrossRef](#)]
59. Xu, Z.; Zhang, L.; Guo, R.; Xiang, T.; Wu, C.; Zheng, Z.; Yang, F. A highly sensitive and selective colorimetric and off-on fluorescent chemosensor for Cu²⁺ based on rhodamine B derivative. *Sensor Actuat B Chem.* **2011**, *156*, 546–552. [[CrossRef](#)]
60. Zhang, J.; Zhang, L.; Wei, Y.; Chao, J.; Shuang, S.; Cai, Z.; Dong, C. A selectively rhodamine-based colorimetric probe for detecting copper(II) ion. *Spectrochim. Acta A Mol. Biomol. Spectrosc.* **2014**, *122*, 731–736. [[CrossRef](#)] [[PubMed](#)]
61. Zhang, J.; Zhao, X.; Liu, X.; Dong, C. Enhanced chemical sensing for Cu²⁺ based on composites of ZIF-8 with small molecules. *RSC Adv.* **2020**, *10*, 13998–14006. [[CrossRef](#)] [[PubMed](#)]
62. Moradi, E.; Rahimi, R.; Safarifard, V. Ultrasound-assisted preparation nanostructures of Cu₂(BDC)₂(BPY)-MOF: Highly selective and sensitive luminescent sensing of THF small molecule and Cu²⁺ and Pb²⁺ ions. *J. Solid State Chem.* **2020**, *288*, 121397. [[CrossRef](#)]
63. Zapata, F.; Caballero, A.; Espinosa, A.; Tarraga, A.; Molina, P. A multifaceted ferrocene-benzobisimidazole derivative: Fluorogenic probe for Pb²⁺ and Zn²⁺ cations and unconventional fluorescence behaviour towards Cu²⁺ metal cations. *Dalton Trans.* **2010**, *39*, 5429–5431. [[CrossRef](#)] [[PubMed](#)]
64. Jin, X.; Gao, J.; Xie, P.; Yu, M.; Wang, T.; Zhou, H.; Ma, A.; Wang, Q.; Leng, X.; Zhang, X. Dual-functional probe based on rhodamine for sequential Cu²⁺ and ATP detection in vivo. *Spectrochim. Acta A Mol. Biomol. Spectrosc.* **2018**, *204*, 657–664. [[CrossRef](#)] [[PubMed](#)]
65. Wang, K.; Dong, E.; Fang, M.; Zhu, W.; Li, C. Construction of hybrid fluorescent sensor for Cu²⁺ detection using fluorescein-functionalized CdS quantum dots via FRET. *J. Fluoresc.* **2022**, *32*, 1099–1107. [[CrossRef](#)] [[PubMed](#)]
66. Zhou, H.; Chai, T.; Peng, L. Bisubstrate multi-colorimetric assay based on the peroxidase-like activity of Cu²⁺-triethylamine complex for copper ion detection. *Dyes Pigm.* **2023**, *210*, 111028. [[CrossRef](#)]

Disclaimer/Publisher's Note: The statements, opinions and data contained in all publications are solely those of the individual author(s) and contributor(s) and not of MDPI and/or the editor(s). MDPI and/or the editor(s) disclaim responsibility for any injury to people or property resulting from any ideas, methods, instructions or products referred to in the content.